Ruprecht-Karls-Universität Heidelberg
Department of Physics and Astronomy

Bachelor Thesis in Physics
submitted by

Fabian Raab

born in Bad Kreuznach (Germany)

2022

Designing and Characterization of a Novel Cryogenic Cyclotron Resonator

This Bachelor Thesis has been carried out by Fabian Raab

at the Max Planck Institute of Nuclear Physics in Heidelberg

under the supervision of

Priv. Doz. Dr. Sven Sturm

Abstract

Resonators are the core of many Penning trap experiments. They are used to cool and detect trapped ions. Current resonators are tedious to manufacture and have limited Q-values. In this work, a new superconducting spiral design for a cyclotron resonator was developed and characterized. The new design is smaller than previous designs, allowing it to be implemented inside of the trap chamber. High Q-values were measured, that surpass the typical value of the old designs by an order of magnitude. An additional test of the resonator in a strong external magnetic field of $280\,\mathrm{mT}$ was conducted, that did not show a reduction of the Q-value. Also a design of a cryogenic amplifier was adapted to fit the posed requirements and then manufactured and tested for its amplification at room temperature, to be implemented together with the resonator in the future.

Zusammenfassung

Resonatoren sind ein Kernstücke vieler Penningfallen-Experimente. Sie werden zum Detektieren und Kühlen gefangener Ionen verwendet werden. Die aktuellen Zyklotron-Resonatoren sind mühsam anzufertigen and habe oft limitierte Güten. In dieser Arbeit wird ein neues supraleitendes Spiralen-Design für Zyklotron-Resonatoren wurde erstellt und wird nun charakterisiert. Das Design ist kleiner also die vorherigen, sodass es möglich ist den Resonator innerhalb einer Fallenkammer zu implementieren. Es würden hohe Güten gemessen, die die Güten vorheriger Designs um einer Größenordnung übertreffen. Ein zusätzlicher Test des Resonators in einem starken, externen Magnetfeld von $280\,\mathrm{mT}$ wurde durchgeführt und es ist keine Verringerung der Güte messbar. Ein Design eines Zyklotron-Verstärkers wurde adaptiert um den gestellten Anforderungen zu passen und anschließend zusammengebaut und dessen Verstärkung bei Raumtemperatur gemessen, um in der Zukunft mit dem Resonator zusammen eingebaut zu werden.

Contents

List of Figures

List of Tables

1 Introduction

1.1 Penning traps

Penning traps are important measurement instruments for state-of-the-art precision experiments in atomic and molecular physics. Examples for that are bound electron g-factor measurements performed by the ALPHATRAP-experiment [1] or atomic mass measurements of different isotopes made at the PENTATRAP-experiment [2]. Another example for a Penning trap setup is the FSU setup for measuring the masses of different isotopes [3]. The values obtained for the g-factor of the bound electron can be used to verify current predictions made by quantum electrodynamics (QED), one of the most precise and best tested quantum theories of modern physics [4].

The Penning trap itself is an ion trap, in which ions can be trapped and stored for later experiments and observations with static fields. Along the trap-axis there is a homogenic magnetic field $\vec{B} = B_z\vec{e_z}$ which is generated by an external superconducting solenoid. This field confines particles with charge q moving with a velocity vector $\vec{v}$ in the radial direction due to the Lorentz force, but provides no confinement in the direction along the trap axis.

$$\vec{F_L} = q \cdot \vec{v} \times \vec{B} = -qv_\rho B_z \cdot \vec{e_\rho} \tag{1.1.1}$$

Due to the traps cylindrical symmetries all unitvectors are given by their definition in cylindrical coordinates and the velocity vector can the be split into a radial component v_ρ and a component parallel to the trap axis v_z such that

$$\vec{v} = v_\rho \cdot \vec{e_\rho} + v_z \cdot \vec{e_z} \quad . \tag{1.1.2}$$

To properly store the charged particles one needs an additional force acting along the trap axis. To achieve this an electrical quadrupole field is applied by a set of electrodes [5]. In a parabolic trap, there are two endcap electrodes and a ring electrode with the opposite polarity of the to-be-trapped particle and an applied voltage of U_0 between the electrodes. This creates a harmonic potential along the trap axis, which can be described with the characteristic trapsize d and the expansion coefficient C_2 [6] via the formula

$$V_{el}(z) = U_0 \frac{z^2}{d^2} \frac{C_2}{2} \quad . \tag{1.1.3}$$

In practice cylindrical trap electrodes [7] are often used because they are easier to manufacture and offer the opportunity to transport particles between different stacked traps. To achieve this despite the altered geometry, additional correction electrodes are needed to obtain this potential. The motion of an isolated particle in the trap is now in the ideal case only influenced by this arrangement of fields. The

resulting trajectory of the ion can be split up into three so called eigenmotions. The magnetron motion with frequency ν_- is the slowest of the three motions and is caused by the drifting of the particle in the $\vec{E} \times \vec{B}$-field. Then only affected by the electric field there is the axial frequency ν_z. The fastest of the three eigenmotions is the modified cyclotron frequency ν_+, which arises from the free cyclotron motion $\omega_c = \frac{q}{m}B$, but is modified due to the drifting of the particle. Using the field configurations of the trap together with the laws of electrodynamics yields the formulas for the frequencies of the three eigenmotions of a charged particle with mass m [5]

$$\omega_z = \sqrt{\frac{qU_0}{md^2}C_2} \tag{1.1.4}$$

$$\omega_\pm = \frac{1}{2}\left(\omega_c \pm \sqrt{\omega_c^2 - 2\omega_z^2}\right) \quad , \tag{1.1.5}$$

with $\omega = 2\pi\nu$. These three frequencies are linked to the free cyclotron motion via the invariance theorem [5], which also holds even if the trap is not perfectly aligned or elliptic with the magnetic field

$$\omega_c^2 = \omega_+^2 + \omega_z^2 + \omega_-^2 \tag{1.1.6}$$

For typical values used in the experiments mentioned above the order of magnitude of the three eigenmotions are for the modified cylcotron frequency $\nu_+ \approx 30\,\mathrm{MHz}$, the axial frequency $\nu_z \approx 600\,\mathrm{kHz}$ and the magnetron frequency $\nu_- \approx 10\,\mathrm{kHz}$.

1.2 The ALPHATRAP-Experiment

The core of the experiment consists of three seperate Penning traps stacked on top of each other. Each of the three traps fulfills a unique purpose for the experiment and is therefore slightly modified from the default setup as mentioned above.

The ions are provided in form of an ion cloud by an electron beam ion trap (EBIT) and are guided via a beamline to the trap. The HD-EBIT setup [8] located at the Max Planck Institute of Nuclear Physics (MPIK) is designed for a beam energy of up to $100\,\mathrm{keV}$ which is enough to produce hydrogenlike lead $^{208}\mathrm{Pb}^{81+}$ [9].

The first part of the trap stack in which the ion cloud enters is the capture trap (CT). Here the cloud is first captured by an electrostatic well produced by various control electrodes as illustrated in Figure 1.1a. The well can be opened on either side to capture the ion cloud and then later to transport individual ions to the other parts of the experiment. To remove unwanted ion species that might have passed previous filters in the beamline, such as the Wien- or time-of-flight filters, they get excited and leave the potential [1]. For this the cloud is transported into the precision trap (PT), which is the next part of the setup.

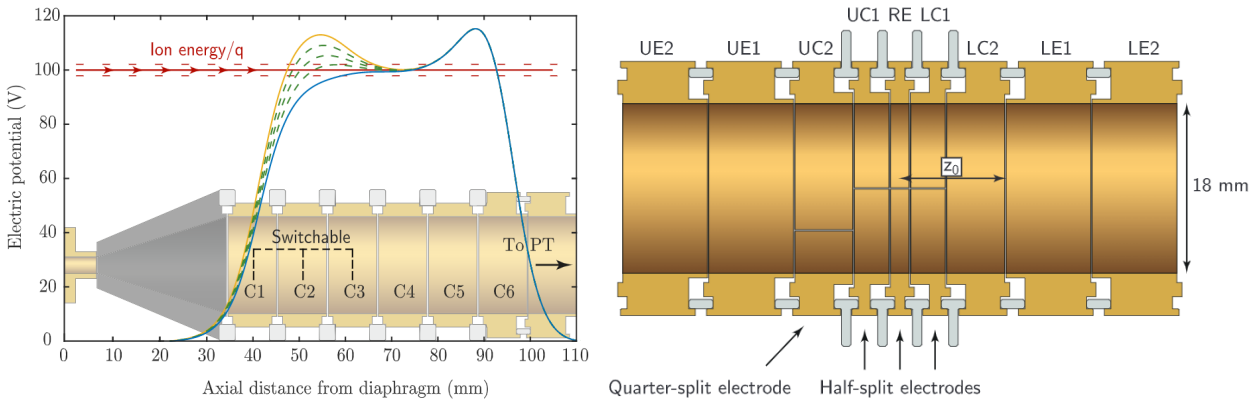

(a) (b)

Figure 1.1: (a) Illustration of the capture trap control electrode configuration and the resulting potentials, (b) Illustration of the precision traps electrode configuration with several correction electrodes ($\mathrm{UC}_{1,2}$, $\mathrm{LC}_{1,2}$) and a ring electrode (RE) in the middle (Taken figures reproduced from [1]).

The PT has a very homogenous magnetic field with field stength $B = 4\,\mathrm{T}$ and is used to precisely measure the cyclotron and Larmor frequency of the ion. To this end the ring electrode is used to pick up the image current of a few $Z \cdot 1\,\mathrm{fA}$ (depending on the charge $Q = Ze$) of the moving ion in the trap center. For the detection of the axial motion of the ion a resonator is connected to the trap. The resonantly enhanced signal is further amplified by a cryogenic amplifier with low noise. Performing a FFT on the signal yields a resonance curve with a dip at the axial frequency [1]. Additionally to the axial resonator, a cylcotron resonator is also connected to the PT. The purpose of this resonator will be explained in the

upcoming subsection.

The third part of the trap stack is the analysis trap (AT). Here, the ring electrode is made out of a ferromagnetic metal which distorts the otherwise homogeneous magnetic field, pulling the field lines towards it. This results in a magnetic field gradient along the trap axis. The magnetic field can then be described in first order by a quadratic dependence on the position along the trap axis with an offset. Given that a particle with magnetic moment $\vec{\mu}$ has an additional potential in a magnetic field $V_{mag} = -\vec{\mu} \cdot \vec{B}$, this modifies the total potential that the ion feels by an addition of the magnetic potential to the electrostatic potential. The modification of the total potential changes the axial frequency [1]. This change is proportional to the magnetic moment $\vec{\mu}$, which can be calculated from quantum mechanics with the total angular momentum $\vec{J}$ of the particle and the g-factor g_j by the formula

$$\vec{\mu} = g_j \frac{q}{2m} \vec{J} \quad . \tag{1.2.1}$$

The total angular momentum of the ion consist out of the magnetic moment of the nucleus and the bound electron(s). This yields an offset in the potential and therefore in the axial frequency which can be corrected by adjusting the voltage applied to the endcaps. For electrons with spin $s_z = \pm\frac{1}{2}\hbar$ the magnetic moment is given by

$$\vec{\mu} = g_s \mu_B \frac{\vec{s}}{\hbar} \tag{1.2.2}$$

with the Bohr magnetron μ_B and the reduced Planck constant $\hbar$. Because of the two spin-states of the electron, there are two energy levels, which is called the Zeeman splitting. The spin state of the electron can be changed by an absorption or stimulated emission of a photon with the right energy.

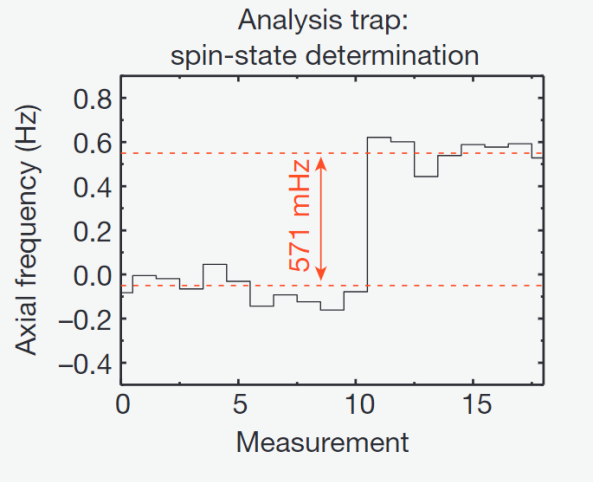

Figure 1.2: Measurement of the axial frequency in the AT to determine the initial spin (Taken from [10])

This energy is given by $E = \hbar\omega_L$, with the Larmor frequency

$$\omega_L = g_s \frac{e}{2m_e} B \tag{1.2.3}$$

The AT is now used to determine the current spin state by repeating the process of measuring the axial frequency and trying to induce a spin-flip or change of the electrons state by irradiating the ion with a the microwave-frequency $\nu_{MW} \approx \nu_L$. This process can be seen in Figure 1.2. To determine the Larmor frequency, the ions will be pulsed in the PT with a MW-pulse close to the theoretically expected Larmor frequency once. The AT will then be used to determine whether this pulse flipped the spin of the electron. This will be repeated for various frequency values of the MW-pulse in an interval around the Larmor frequency. From these measurements one can get the flip probabilty depending on the frequency of the MW-pulse, which results in a plot depicting a resonance curve with its maximum at the Larmor frequency [10]. Together with the measurement of the cyclotron frequency in the PT the magnetic field can be eliminated for the calculation of the g-factor.

$$g = 2\frac{\omega_L}{\omega_C}\frac{q}{e}\frac{m_e}{m_{ion}} \tag{1.2.4}$$

The g-factor is therefore determined by only measuring frequencies, while e and the ion masses have to be taken from other independent measurements.

1.3 Cyclotron resonators

The resonator can be used for different tasks. It can be used as a detector for a certain frequency, as it is done for the axial resonators in the ALPHATRAP setup [1]. Another use can be cooling. If the resonator itself is cooled to a low temperature, it can cool the ions motion if the motional frequency matches the resonators frequency. Such an resonator is formed from a low-loss inductor and the parasitic capacitance of the trap electrodes. This can then be simplified to a parallel circuit with only a parallel resistance R_p representing any losses in the circuit, a coil with inductance L and a capacitor with capacitance C. The circuits impedance can be calculated from the rules for a parallel circuit

$$Z_{\text{tot}}(\omega) = \frac{1}{\frac{1}{i\omega L} + i\omega C + \frac{1}{R_p}} \quad . \tag{1.3.1}$$

For low damping this yields a resonance frequency of $\omega_0 \approx \frac{1}{\sqrt{LC}}$. Another important value for a resonator is the so called Q-value. It is a measure for how much energy got lost in the circuit due to dissipation after one oscillation.

$$Q = 2\pi \frac{\text{Total energy of oscillation}}{\text{Energy lost after one oscillation}} = 2\pi \frac{E_{\text{tot}}}{E_{\text{loss}}} \quad . \tag{1.3.2}$$

The energy in the system is stored in the magnetic and electric fields which oscillate. It can be calculated from the amplitudes of the flowing current $\hat{I}$ or the voltage $\hat{U}$:

$$E_{\text{tot}} = \frac{1}{2}C\hat{U}^2 = \frac{1}{2}L\hat{I}^2 \tag{1.3.3}$$

The energy lost during an oscillation of length $T = \frac{2\pi}{\omega_0}$ can be calculated from the power flowing through the equivalent series resistance (ESR) R_{ESR} of the inductance.

$$E_{\text{loss}} = \int_0^T U(t)I(t)\text{dt} \tag{1.3.4}$$

Because the phase difference of the voltage applied at and the current flowing through this series resistance is zero one can simplify further to

$$E_{\text{loss}} = \int_0^T \hat{I}^2 R_{\text{ESR}} \cos^2(\omega_0 t)\text{dt} = \frac{\hat{I}^2 R_{\text{ESR}}\pi}{\omega_0} \quad . \tag{1.3.5}$$

In total this results in the following formula for the Q-value

$$Q = \frac{\omega_0 L}{R_{\text{ESR}}} \quad . \tag{1.3.6}$$

For an application in a non-ideal environment also losses in dielectrical materials R_d and potential shielding materials R_s close to the resonator have to be accorded for by summing the individual effective resistances. The losses can be described by additional resistors in series to the ESR such that

$$Q = \frac{\omega L}{R_{\text{ESR}} + R_s + R_d} \quad . \tag{1.3.7}$$

Besides the definition of the Q-value from the energies there is also a definition from the resonance frequency ω_0 and the full width half maximum (FWHM) $\Delta\omega$ of the power spectrum

$$Q = \frac{\omega_0}{\Delta\omega} \quad . \tag{1.3.8}$$

This can be motivated from the Fourier transform, similar to calculations made in chapter 4. These definitions are only equivalent for weakly damped systems, or systems with a high Q-value. The cooling time constant is inversely dependent on the Q-value, so a high Q-value results in a low total cooling time [11]. Cooling the cyclotron frequency directly can bring the cyclotron motion to the temperature of the resonator. If cooling is done via sideband coupling with a directly cooled axial motion, only the axial motion can be cooled down to the temperature of the resonator. For the typical frequencies of the three eigenmotion listed in subchapter 1.1, cooling the axial motion down to $4\,\text{K}$ will leave the

cyclotron motion at about $160\,\mathrm{K}$ [1]. A large bandwidth could also mean that other sidebands which have frequencies close to the cyclotron frequency might be hit, which could lead to unwanted excitations. Having a high Q-value increases the need for high precision in the manufacturing process. The higher the Q-value, the smaller the bandwidth and the more precise the resonance frequency has to fit to the ions motional frequency, if the ions motional frequency cannot easily be tuned.

Cyclotron resonators with a high Q-value are hard to build and it is possible that the Q-value significantly decreases over time and over multiple cooldowns. The manual manufacturing process of classical helical resonators is very time consuming and the resulting Q-values are mostly not very well predictable [12]. Due to potential imperfections in the helical shape and different behaviours during the cooldown phase in the experiment, the Q-value and the resonance frequency can also vary quite unpredictably from room temperature to the $4\,\mathrm{K}$ environment, due to differences in the materials reaction during the cooldown [12].

The goal of this work is therefore to create a cyclotron resonator which has a high Q-value that is also more predictable and stable than previous resonator designs. It should also be smaller than previous designs, giving it the possibility to be directly built into the inner trap chamber. The smaller size will also reduce the thermal mass that has to be cooled.

2 Material and design

In this section the motivation behind the choice of material and design will be explained

The general properties of the resonator are inspired by this reference [13]. The resonator should be made out of a material with very low resistance and all dielectric material close to the wire should also have a good loss tangent. Because the resonator will be cooled in the experimental setup, it can be build from superconducting material to minimize the losses from the wire. Yttrium-Barium-Copper-Oxide (YBCO) is a high-temperature superconductor (HTS) with a critical temperature of up to $T_{\text{crit}} = 96\,\text{K}$ depending on its oxygen content [14]. To test a resonator made out of this material one could use liquid nitrogen which has a boiling temperature of $T_{\text{LN2}} = 77\,\text{K}$. Since YBCO can be deposited as a thin film on wafers and different substrates, this opens up the possiblity to use lithographic tools to construct a planar coil. To ensure the superconductivity and reduce waiting times the substrate should also have a high thermal conductivity to allow a quick thermalization. If this dielectric material would fill the volume surrounding the spiral the loss tangent is defined by

$$\tan(\delta) = \frac{R_{\text{ESR}}}{|X_c|} = \omega C R_{\text{ESR}} \quad , \tag{2.0.1}$$

with the capacitive reactance X_c. In this case the limiting Q-value for the dielectricum is just the inverse of the loss tangent. If the material only inhabits portions of the volume around the resonator the limit for the Q-value will be higher. Sapphire has very good properties for both requirements. The thermal conductivity at room temperature is approximately $\lambda_{\text{sapphire}} \approx 40\,\frac{\text{W}}{\text{mK}}$ [15], which is only one order of magnitude lower than copper [16]. For lower temperatures down to about $10\,\text{K}$ the thermal conductivity is better than copper [17]. With a loss tangent at a frequency of $\nu = 22\,\text{GHz}$ and at room temperature of about $\tan(\delta)_{\text{sapphire}} = 10^{-5}$, which decreases by up to three orders of magnitude for a temperature of $10\,\text{K}$ [18], sapphire is perfectly suitable as a substrate.

The designing process was already done in my "Projektpraktikum" here at the MPIK. Because of that, I will only shortly summarize the most important parts and give more details in subsection A.1 of the appendix. The shape of choice for the resonators is a circular spiral with four defining properties which determine the final inductance of the spiral calculated by the modified Wheeler formula [19] for the octogonal shape, which is closest to the circular shape. These properties are the amount of turns N, the outer diameter d_{out}, the turn spacing s and the width w of the wire as illustrated in Figure 2.1. A reason for choosing the circular spiral over other shapes like a quadratic spiral is that there will be less imperfections in the shape, which for a quadratic spiral would arise in the corners due to the lithographic manufacturing process. Also the magnetic field will be more easily describable for a circular spiral. Due to implementations in different experimental setups and for different ion species a set of frequencies ν_0 was chosen together with the total parallel capacitance C_{par} given be the trap setup. From these the targeted inductance can be calculated. Table 1 lists those quantities together with the inductance

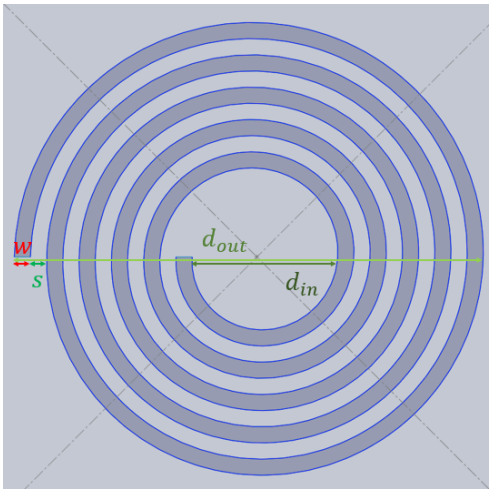

Figure 2.1: Sketch of a spiral, showing all defining properties to calculate the inductance. The number of turn and the inner diameter are interchangeable as a parameter, because they are linked via the other three parameters.

calculated from the modified Wheeler formula for the chosen set of parameters.

ν_0 [MHz]	C_{par} [pF]	L_{target} [nH]	L_{Wheeler} [nH]
6.8	20	24651	24864
17.9	10	7115	7158
18.4	10	6734	6701
20.4	20	2739	2763
27	20	1564	1567
28	20	1454	1439

Table 1: Comparison of the targeted inductance and the calculated inductance.

It will later be easy to add parallel capacitors to the circuit to tune the frequency. This will increase to total capacitance of the circuit and therefore reduce the resonance frequency. To account for potential deviation from the desired inductance because of the approximate calculation with the modified Wheeler formula and errors in the manufacturing process in advance, the target inductance is 10% lower than the inductance one would get from plugging in the desired resonance frequency and the given trap capacitance. This leaves a threshold of $+11.\bar{1}\%$ for the parallel capacitance. There were three additional designs made, which are intended to exclude soldering directly on top of the sapphire wafer like in Figure 2.2.

For these designs the total inner area of the spiral is used for a capacitive coupling. Additionally the outer pad is replaced by a ring around the resonator, which has the same area as the inner circle. This is made, to simplify the equations involved for the calculation of the total parallel capacitance of the

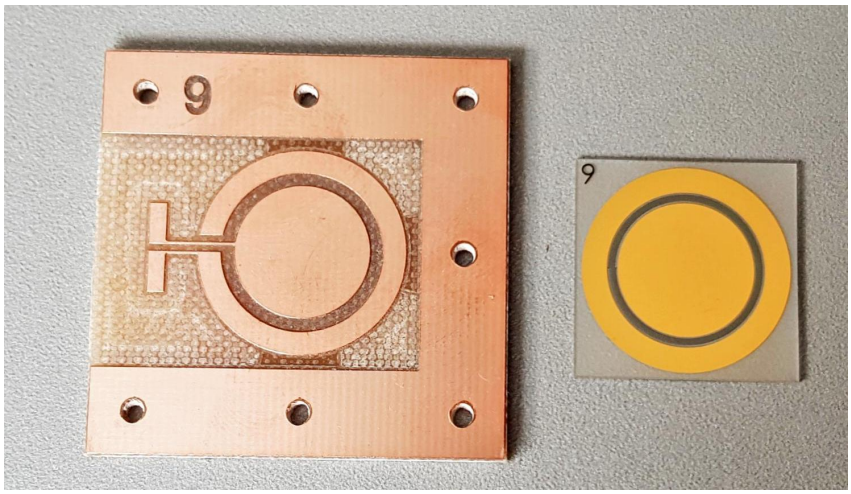

Figure 2.2: Picture of the design for capacitive coupling. This prevents the need to solder directly on top of the gold-coated YBCO. The right side shows the resonator and the left side the opposite planes to form the capacitor. The coil is the black area between the outer ring and the inner circle.

resonator. More details on these designs can be found in subsection A.2 of the appendix.

The different designs were then given to an external company [20], which was tasked to manufacture the wafers with the superconducting spiral on top. For the purpose of soldering later there are two pads with size $2\,\mathrm{mm}$ by $6\,\mathrm{mm}$ included in the design, one on the inside of the spiral and one on the outside. For some designs the pads inside of the spiral had to be a little bit smaller to fit. The sapphire wafer, on which the YBCO film with thickness $350\,\mathrm{nm}$ is placed on top, is $0.5\,\mathrm{mm}$ thick. For the pads there is an extra layer of gold coating with thickness $200\,\mathrm{nm}$ deposited on top of the YBCO. Because of the thin sapphire wafer and the sub-micrometer YBCO and gold layers, handeling the resonator has to be done very cautiously. For the total of nine resonators and all these processes the price for our prototypes sums up to $1.680\,€$ or correspondingly $187\,€$ per resonator.

3 Calculations with COMSOL

In this chapter the inductances calculated from the targetted resonance frequency and the given trap capacitance are compared to a simulation of the resonator in COMSOL. This simulation also yields some information about the magnetic field which will be useful later.

3.1 Validation of the calculated inductance

To verify the inductances a model of the resonator was implemented into COMSOL. This model is made such that the free parameters of the spiral, mentioned in the previous chapter and the thickness of the YBCO film are free parameters. A picture of this model is shown in Figure 3.1

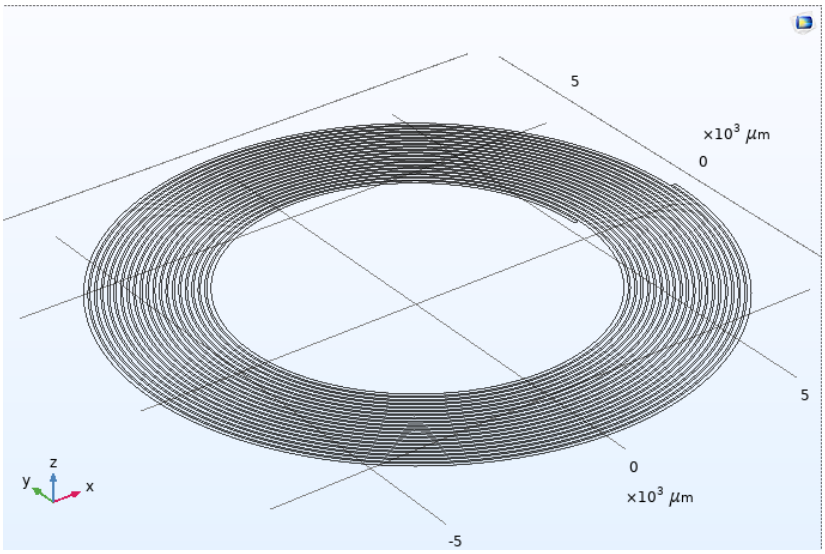

Figure 3.1: Spiral with finite thickness created in COMSOL

The reason behind having the height of the film as a free parameter is because the true film height of $h = 350\,\mathrm{nm}$ is not feasable to simulate, due to meshing difficulties. Using this height would result in a very detailed mesh, which would need hours of time for one simulation. For the resonators with resonance frequencies $\nu_0 = 17.9\,\mathrm{MHz}$ and $\nu_0 = 27\,\mathrm{MHz}$ there were two parametric sweeps simulates to estimate the influence of the changed thickness on the result of the simulation. The values chosen for the thickness h are

$$h[\mu\mathrm{m}] \in \{2, 2.5, 3, 3.5, 4, 4.5, 5, 10, 20, 50, 100, 200, 500\} \quad . \tag{3.1.1}$$

For the simulation the module "Magnetic Fields, Currents Only" was used and the simulation parameter yielding the inductance was read and plotted for the various values of the thickness. The results of the

simulation can be seen in Figure 3.2

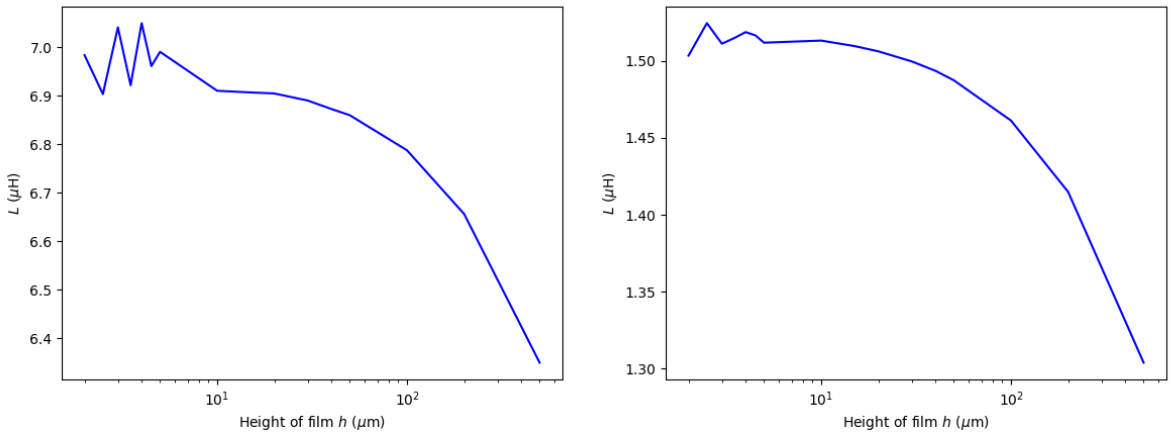

(a) (b)

Figure 3.2: Results of different simulations varying the thickness of the YBCO film using COMSOL. (a) For the parameter of the designs with $\nu_0 = 17.9\,\mathrm{MHz}$. (b) For the parameter of the designs with $\nu_0 = 27\,\mathrm{MHz}$. More details are explained in the text.

Here one can see a significant reduction of the inductance for a larger thickness of the YBCO film. Due to the scaling of the inductance with the volume the magnetic field can spread to, it is expected that one will observe a reduction of the inductance, if the thickness of the film gets significant in comparison to the length scales of the wire. For the first seven data points the inductance is fluctuating slightly, but on average is very flat. These fluctuation might be due to numerical uncertainties and are not visible for the later data points, because they are much more sparse. Both graphs also show the same trend, from which one can extrapolate, that the value of the inductance at the true thickness will only vary by a few percent, if one takes a thickness of $h = 5\,\mu\mathrm{m}$ for the simulation.

For the simulation of the magnetic field and the inductance L_{COMSOL}, the spiral was fed with a current of $I = 1\,\mathrm{A}$ flowing through the whole cross-section from the outer end. The simulation was performed in a volume which is much larger than the resonator. This was then done for all designs and compared to the initial target inductances L_{target}. For better comparison the deviation of the simulated inductance to the targeted inductance was also calculated in percent, as shown in Table 2

The deviations in Table 2 are all below $+11.\bar{1}\%$, which is the threshold mentioned in chapter 2 left for finetuning with exterior parallel capacitors. Most designs have lower inductances than the target inductance, which can be explained by the thicker film height chosen for the simulation. The deviation for the resonators at $27\,\mathrm{MHz}$ and $28\,\mathrm{MHz}$ is noticeably larger than for the other ones. These two resonators are also the ones with the smallest outer diameter and thus might start to deviate earlier to lower values than the other designs, as discussed above. Overall one can see that the simulation fits within 10% of the

ν_0 [MHz]	L_{COMSOL} [nH]	L_{target} [nH]	Deviation [%]
6.8	25046	24651	1.6
17.9	7001	7115	-1.6
18.4	6673	6734	-0.9
20.4	2709	2739	-1.1
27	1512	1564	-3.3
28	1363	1454	-6.3

Table 2: Comparison of the target inductances with the simulated inductances made with COMSOL. From the extrapolation of the thickness of the spiral a relative error of about 2% can be estimated.

given target value. No further errors are specified and no rounding was done for in this part, because the goal was to be able to identify whether the inductances one could expect to get from the created spirals will fit to the simulation.

3.2 Estimation of influences on the Q-value

To estimate the influence of nearby materials on the losses and therefore the Q-value, it is useful to look at the magnetic field and its strength at different points around the resonator. Along the z-axis, which is perpendicular to the resonators plane and centered in the middle of the resonator, the strength of the magnetic field can be calculated from the law of Biot-Savart

$$\vec{B}(\vec{r}) = \frac{\mu_0}{4\pi} \int \vec{j}(\vec{r}') \times \frac{\vec{r} - \vec{r}'}{|\vec{r} - \vec{r}'|^{\frac{3}{2}}} \mathrm{d}^3 r' \quad , \tag{3.2.1}$$

assuming that the spiral is made out of N ring currents with radii R_n. Each ring current can approximately be described by an infinitessimal thin ring current density given by

$$\vec{j}(r, \phi, z) = I\delta(r - R_n)\delta(z)\vec{e}_\phi \tag{3.2.2}$$

with the applied current I, the Dirac delta $\delta(x)$ and the unity vector in cylindrical coordinates $\vec{e}_\phi$. Evaluating the integral in cylindrical coordinates for this ring current at $r = 0$ results in

$$\vec{B}_n(z) = \frac{\mu_0 I}{2} \frac{R_n^2}{\sqrt{R_n^2 + z^2}^3} \vec{e}_z \quad . \tag{3.2.3}$$

The total magnetic field along the z-axis is then given by the sum over all N ring currents.

Along the radial direction it is not possible to calculate the dependence of the magnetic field strength against the radial distance from the center that easily due to the loss of angular symmetry along the integration path. The magnetic field resulting from the simulation was plotted along two directions.

Both graphs can be seen in Figure 3.3 and show the absolute value of the magnetic field strength. For the z-direction, the result from the equation above is also plotted for comparison.

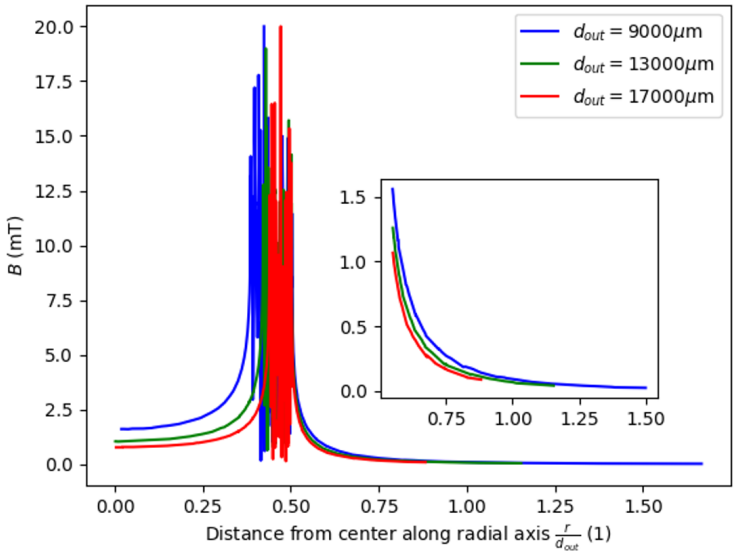

(a)

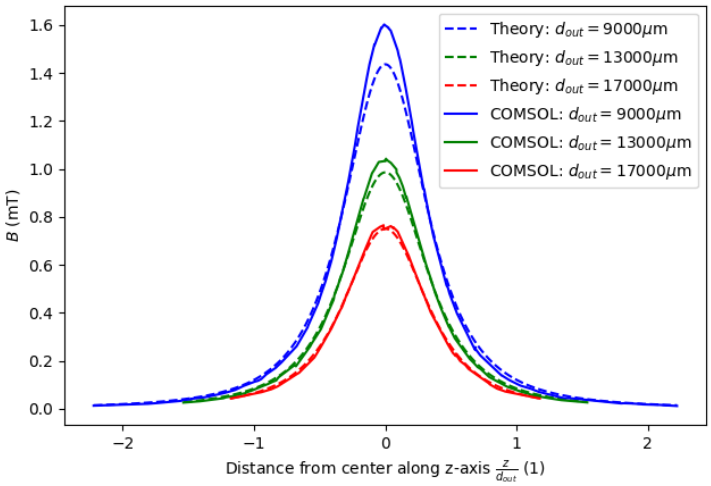

(b)

Figure 3.3: Plots from the COMSOL simulation and the analytic calculation based on the law of Biot-Savart. The graphs are normalized by the outer diameter d_{out} of the spiral, thus the B-field is plotted against $\frac{x}{d_{\text{out}}}$ (a) With $x = r$ for the radial direction. (b) With $x = z$ for the z-direction

In Figure 3.3a one can clearly see the position of the resonator, which ends at $\frac{r}{d_{\text{out}}} = 0.5$. From this plot only the B-field outside of the resonator, so for $\frac{r}{d_{\text{out}}} \geq 0.5$ is interesting, because there will not be

any material other than sapphire for $z = 0$ inside of this bound. This is plotted in the zoomed plot, which starts at $\frac{r}{d_{\text{out}}} = 0.55$. One can see that at $\frac{r}{d_{\text{out}}} = 1$, a distance of half the spirals outer diameter, there is almost no field present anymore. Figure 3.3b shows that the analytic calculation is quite close to the simulation of COMSOL. It underestimates the magnetic field in the center of the resonator and is a bit broader. In the simulation the coil is not idealized, meaning the wire is not infinitesimally small in its cross-section. The theoretic calculation also approximated the spiral by rings which also contributes to some errors. In general, one can see that the for smaller resonators the magnetic field stretches further away compared to the resonators outer diameter. A safety region, where conductive materials should be avoided, can be estimated at one times the outer diameter above and below the resonator. For positions in space with $z \neq 0$ and $r \neq 0$ the magnetic field will always be lower than at the corresponding position with $z = 0$ which is depicted in Figure 3.3b. So if one keeps a cylinder with radius $r = d_{\text{out}}$ and height $h = 2d_{\text{out}}$ free of any material with high losses, the Q-value should not be significantly reduced.

3.3 Estimation of influences on the inductance

The inductance is directly connected to the energy stored in the magnetic field lines

$$E_{\text{mag}} = \frac{1}{2} L I^2 = \frac{1}{2\mu_0} \int \vec{B}^2 \mathrm{d}V \quad . \tag{3.3.1}$$

Given the simulations from the previous subchapter with $I = 1\,\mathrm{A}$, COMSOL can calculate the inductance L from the integral over a defined cylinder volume with radius R and height h centered at the resonator with

$$L = \frac{1}{\mu_0} \int \vec{B}^2 \mathrm{d}V \quad . \tag{3.3.2}$$

In a conductor enclosing the resonator induced currents will form due to the rapidly alternating magnetic field radiated out by the resonator. Because the resonator has a resonance frequency at a few $10\,\mathrm{MHz}$ the induced currents will not be able to decay, so the conductor permanently shields the outside from the magnetic field generated by the resonator. If one now identifies the boundaries of the integration volume as the casing made out of a certain conductor, one can estimate the change of the inductance due to this boundary condition. The integration was performed for serveral volumina with $\frac{r}{d_{\text{out}}}$ and $\frac{z}{d_{\text{out}}}$ each ranging between 0.6 and 2, in steps of 0.2. The design used for this simulation (see Figure 3.4) is the design for the $27\,\mathrm{MHz}$ resonator, but with an outer diameter $d_{\text{out}} = 17\,000\,\mu\mathrm{m}$.

In this plot the black striped area visualizes all casing that would be at least partly inside of the cylinder of high influence. The inductance for the casing with $r = d_{\text{out}}$ and $h = 2d_{\text{out}}$ (or $z = d_{\text{out}}$) is reduced to $L_{\text{casing}} = 3.545\,\mu\mathrm{H}$ from the value without any casing $L_{\text{free}} = 3.583\,\mu\mathrm{H}$. This is a reduction of only 1.1%, which is negligible. For higher casings or ones with a larger radius this deviation will

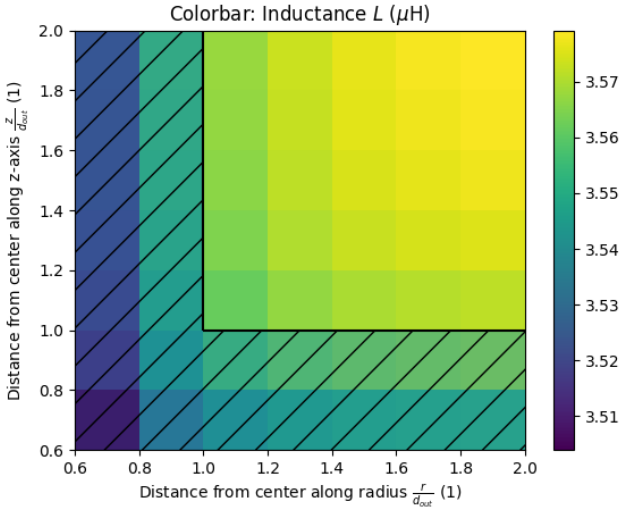

Figure 3.4: COMSOL simulation of impact on inductance for different casing sizes. The black area markes the sets of parameters for r and z such that the casing would be inside of the cylinder of high influence.

become even smaller, because less of the field gets blocked. From this the minimum dimensions for a casing can be estimated.

4 Measurements

In this chapter the setup of the measurement for different resonators, the results and their discussion are presented.

4.1 Tests of the unloaded resonator at Mainz

The idea of a superconducting resonator implemented as a spiral made out of YBCO on a sapphire substrate was also advanced by a group at the Johannes-Gutenberg University in Mainz lead by Dr. Christian Smorra [21]. They designed a planar square spiral resonator for a similar resonance frequency. Because the resonators in Mainz arrived a few weeks earlier than ours, I had the opportunity to join the group for a few weeks to help them test their resonators. It was also possible to test the resonator in a strong magnetic field up to $280\,\mathrm{mT}$ [22], which was not possible at the MPIK in the time given.

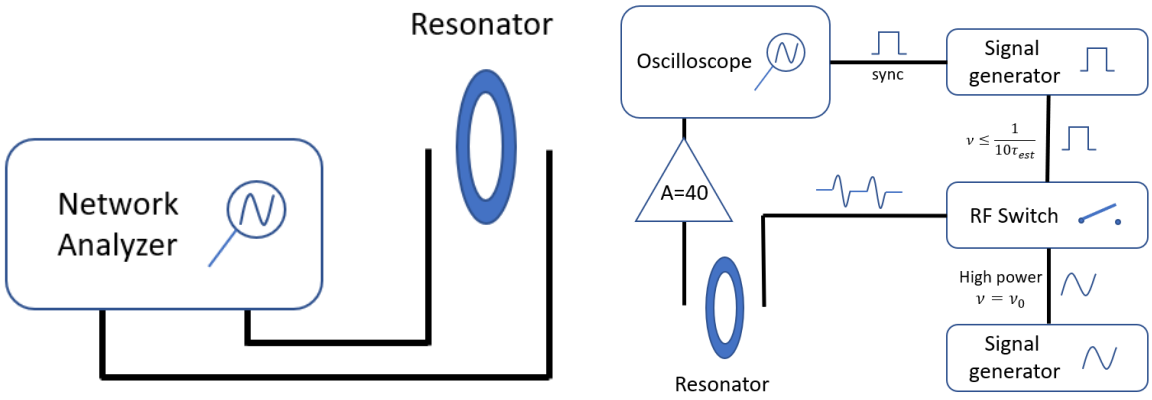

(a) (b)

Figure 4.1: The two different measurement setups. (a) Uses just a network analyzer to determine the Q-value (b) Is a setup for a ring-down measurements which is described in more detail in the text

There are two general setups used to determine the Q-value as illustrated in Figure 4.1. The first setup as shown in Figure 4.1a uses a network analyzer to measure to response of the resonator at different excitation frequencies. In total, there are two antennas installed close to the resonator, one for each pad. Each antenna is connected to one port of the network analyzer. The antennas are made out of semi-rigid coax cables to reduce cross-talk between the transmitter and receiver and to ensure stability during the tests. At the end of the antennas the shield is removed and the signal cable is isolated with PTFE to exclude accidental contacts to materials close by. The network analyzer is then run in the S21 mode which defines the antenna connected to port 1 as the transmitter and the antenna connected to port 2 as the receiver. It will sweep over the set interval of frequencies and calculate the fraction of power received

P_{rec} divided by the power sent P_{sent} for each frequency in decibel which is defined by

$$L[\mathrm{dB}] = 10 \log_{10} \left(\frac{P_{\text{rec}}}{P_{\text{sent}}} \right) \quad . \tag{4.1.1}$$

The spectrum analyzer will then be able to measure the FWHM of the resonance. This corresponds to the width at $3\,\mathrm{dB}$ below the maximum.

To cool the resonator below its critical temperature, a pulse-tube refrigerator ("coldhead") was used. A good mechanical connection to reduce vibrations induced by the coldhead itself and other sources and a good thermal connection to the coldhead has to be ensured. Expecially the mechanical connection to the coldhead was changed in multiple iterations of the measurement to reduce losses induced in the surrounding material which limited the Q-value. These different iterations and their results will be described later in this chapter. The total direct current resistance at room temperature from one end of the spiral to the other end was measured to be $R_{\text{w}} = 92\,\mathrm{k}\Omega$, which shows that the resonator will not be visible before its temperature surpasses the critical temperature, because the losses will be very high and therefore the Q-value very low. Such a high resistance is also expected because YBCO has a resistivity of $\rho = 1.6 \times 10^{-1}\,\Omega\mathrm{m}$ at room temperature [23], which is seven orders of magnitude higher than the resistivity of copper at room temperature. Before the coldhead was started, the cross-talk of the two antennas was measured, to later be able to distinguish the resonance from other features in the cross-talk more easily. Because in this setup the resonator is not connected to anything, the parallel capacitance is determined by the coupling capacitances of the antenna and the self capacitance of the spiral. Since the designed resonance frequency is intended to be achieved when connected to the trap, which adds a capacitance of $10\,\mathrm{pF}$ to $20\,\mathrm{pF}$ depending on the design, the resonance frequency of the unloaded resonator will be significanty different. Assuming a lower bound for the self capacitance of about $1\,\mathrm{pF}$, the resonance frequency could be a factor of five higher. Knowing this, one also has to look at higher frequencies on the network analyzer.

For high Q-values the FWHM of the resonance becomes very small and can be more easily disturbed by exteriour vibrations like the $2\,\mathrm{Hz}$ pumping of the coldhead. To eleminate such artifacts which might broaden the resonance depicted by the network analyzer, a so called ring-down measurement can be performed. The corresponding setup for this is shown in Figure 4.1b. For this measurement a connection between the Q-value of the power spectrum measured by the network analyzer and the ring-down measurement has to be found. Here, the resonator is excited by a signal generator with the resonance frequency ν_0 measured by the spectrum analyzer. The excitation is then stopped and the resonator oscillates freely and dissipates its energy due to losses resulting in a decay of the signal. The potential difference between the ends of the resonator oscillates with

$$U(t) = U_0 \exp\left[\left(i\omega_0 - \frac{1}{\tau} \right) t \right] \quad t \geq 0 \quad . \tag{4.1.2}$$

where τ is the lifetime of the oscillation and U_0 the initial amplitude. The free decay starts at $t = 0$.

The power spectrum is the graph of the magnitude plotted against the frequency and is what one can observe on the network analyzer. It is defined as the absolute square of the fourier transform of the signal.

$$\mathcal{P}(\omega) = |\mathcal{F}[U(t)]|^2 \tag{4.1.3}$$

$$= \left| \frac{U_0}{\sqrt{2\pi}} \int_0^\infty \exp\left[\left(i(\omega_0 - \omega) - \frac{1}{\tau} \right) t \right] \mathrm{d}t \right|^2 \tag{4.1.4}$$

$$= \frac{U_0^2}{2\pi} \frac{1}{(\omega - \omega_0)^2 + \left(\frac{1}{\tau}\right)^2} \tag{4.1.5}$$

This is equal to the lorentzian curve for the special case that $\omega \approx \omega_0$ and $\gamma \ll \omega_0$ which is defined with the FWHM γ as

$$f(\omega|\omega_0, \gamma) \propto \frac{1}{(\omega - \omega_0)^2 + \left(\frac{\gamma}{2}\right)^2} \quad . \tag{4.1.6}$$

Due to the high Q-values that are expected from this resonator it is sensible to assume $\omega \approx \omega_0$. The lifetime will be in the order of microseconds for Q-values higher than 1000 and frequencies of about $100\,\mathrm{MHz}$. This is much longer than the time of one oscillation which is at $100\,\mathrm{MHz}$ only $10\,\mathrm{ns}$. From these equations one can get $\gamma = \frac{2}{\tau}$ and with Equation 1.3.8 calculate the Q-value from the decay of the signal

$$Q = \pi \nu_0 \tau \quad . \tag{4.1.7}$$

The signal generator with a sinusoidal signal at $\nu_{\text{sine}} = \nu_0$ should have a high peak to peak voltage to ensure that the signal of the decaying oscillation can be resolved. Subsequently, the signal is shut off for a period of time to let the resonator oscillate freely. To this end a second signal generator is used, which sends out a square pulse variing between $0\,\mathrm{V}$ and $5\,\mathrm{V}$ with a frequency $\nu_{\text{square}} \leq \frac{1}{10\tau_{\text{est}}}$. Here τ_{est} is an estimate of the lifetime, calculated from the Q-value given by the network analyzer. The factor 1/10 is made to give the resonator enough time to be able to observe at least one lifetime even if the Q-value is significantly higher than the estimated value. The square pulse and the sinusoidal signal is fed into a RF-switch, which shuts of ν_{sine} if it receives a signal of $5\,\mathrm{V}$ and opens the gate for no signal or $0\,\mathrm{V}$. The result is a sinusoidal signal which is multiplied by a square pulse signal of height one. This signal is then emitted from one of the two antenna. The receiver antenna is connected to an oscilloscope which is triggered by the sync-signal of the signal generator sending out the square pulse signal. Between antenna and oscilloscope a series of amplifiers with a combined amplification of $A = 40\,\mathrm{dB}$ was used to increase the amplitude of the signal such that it will be in a range where the oscilloscope can easily detect the

signal.

4.1.1 First iteration

There were three iterations of the setups in total. In the first iteration, the resonator was mounted in a prefabricated casing made by the group in Mainz. The resonator was put into a very tight copper casing, leaving only about $1\,\mathrm{mm}$ of space between the surface of the resonator and the casing to the top and $0.5\,\mathrm{mm}$ to the bottom. The resulting Q-value and resonance frequency of the first iteration at $4\,\mathrm{K}$ were

$$Q^{(1)} \approx 600 \tag{4.1.8}$$

$$\nu_0^{(1)} \approx 37.13\,\mathrm{MHz} \quad . \tag{4.1.9}$$

During the warmup of the resonator a few data points of the change in Q-value were taken and plotted against the temperature measured by a temperature sensor directly connected thermally to the casing. Because this was not planned initially and the heat capacity of copper is small for low temperatures, the measurement of the Q-value versus the temperature only started at about $40\,\mathrm{K}$ as shown in Figure 4.2.

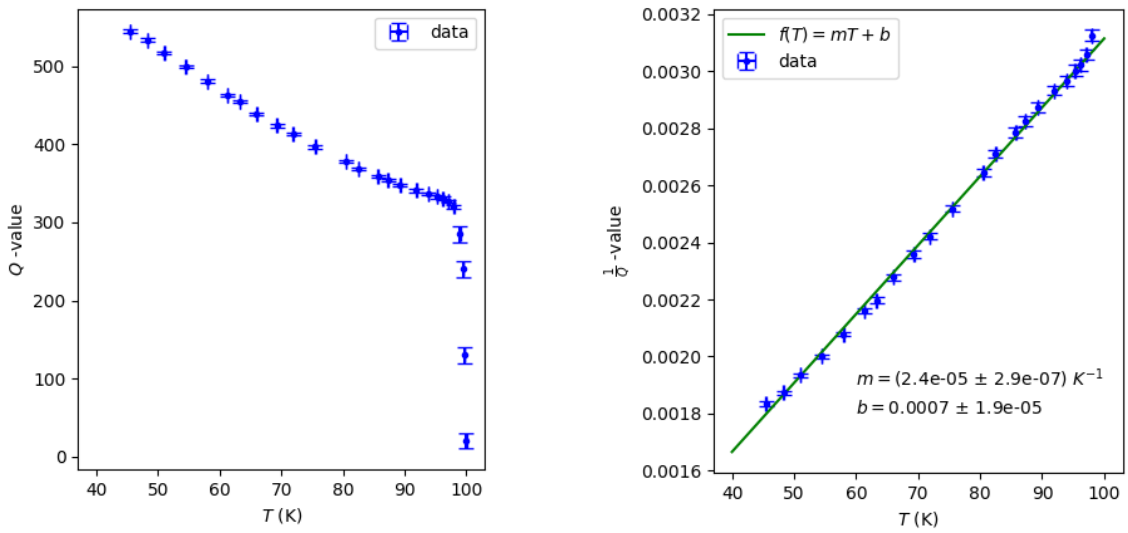

(a) (b)

Figure 4.2: (a) Measurement of the Q-value during the warmup of the first iteration. (b) Plots the inverse Q-value for the datapoints below the critical temperature.

The plot shows a sharp decrease of the Q-value to approximately zero after the temperature has risen to $98\,\mathrm{K}$. This transition is the superconducting YBCO surpassing its critical temperature and becoming normally conducting. The temperature might be a bit higher than the critical temperature of the YBCO because the sensor is mounted on the outside closer to the coldhead experiencing a temperature gradient

from there to the resonator. The calibration of the temperature sensor, specifically in this intermediate range, could also be slightly inaccurate, leading to an error of a few degrees.

As long as the YBCO is operated below its critical temperature, its resistance can be assumed negligible compared to copper. Because of the low loss tangent of sapphire the losses due to the dielectricum are also negligible, leaving the shielding material as the main cause for the observed losses. The datapoints below the critical temperature resemble the function $\frac{1}{T}$ which can be verified by fitting the inverse of the Q-value to a linear function as done in Figure 4.2b. For a pure material like copper, the resistivity increases linearly in T for temperatures above $\gtrsim 0.15\theta$ with the Debye-temperature θ of the material [24]. For the Debye temperature of copper $\theta_{\mathrm{Cu}} = 303\,\mathrm{K}$ this starts at about $45\,\mathrm{K}$ [24]. Due to the estimations made in chapter 3.2, the copper casing strongly limits the Q-value, because of its close proximity to the resonator. The linearity of the inverse Q-value in the temperature regime in which copper is expected to have the linear dependence in its resistivity, is a second indication for the limitations to stem from the copper.

4.1.2 Second iteration

In the second iteration the casing was not used to enclose the resonator, but to hold the resonator on the outside as depicted in Figure 4.3.

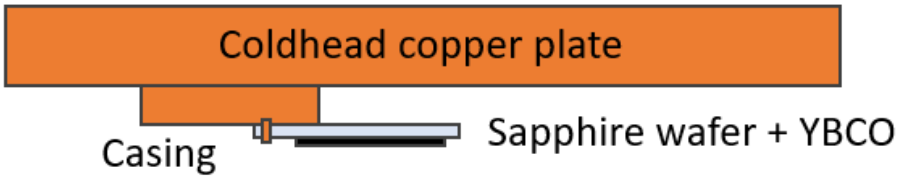

Figure 4.3: Visualization of the setup in the second iteration. The YBCO spiral (black) still partially overlaps with the copper casing. Further details are described in the text.

However, even in this setup a few parts of the spiral still overlapped with the copper, because the distance between the edge of the casing and the holes in the casing, on which the resonator could be tightened on, was too long. The resonator is therefore aligned parallel to the copper plate of the coldhead, with a distance of about half a centimeter. During the process of fastening the resonator on the outside of the casing, the sapphire substrate broke. This also broke the spiral, such that the resonator was no longer useable. Therefore another resonator of a different design, which has a higher resonance frequency, had to be taken for the test. For this setup the resonance frequency and the Q-value was measured with the

network analyzer first.

$$Q^{(2)} \approx 3400 \tag{4.1.10}$$

$$\nu_0^{(2)} \approx 83.567\,\mathrm{MHz} \tag{4.1.11}$$

With these a ring-down measurement was set up as explained above. The results can be seen in Figure 4.4.

In Figure 4.4a the pink line represents the sync-trigger from the signal generator. This line starts at the left marker position. One can see that the signal received by the oscilloscope did saturate before the excitation was shut of at a peak-to-peak voltage determined by the amplifiers, the coupling strength of the antenna to the resonator and the power of the initial excitation. From the oscilloscope a few datapoints were read out using the marker tool. These points are then fitted with an exponential decay, which can be seen in Figure 4.4b. Using Equation 4.1.7 the Q-value can be calculated to be

$$Q_{\mathrm{rd}}^{(2)} = 3400 \pm 250 \quad . \tag{4.1.12}$$

This value is in good agreement with the value from the network analyzer.

As expected, reducing the copper in close proximity yields a higher Q-value. Nevertheless this cannot directly compared to the previous result, because the resonator had to be changed and the resonance frequency therefore different.

4.1.3 Third iteration

To reduce the losses in copper even more the resonator was put into a casing made of Niobium-titanium (NbTi), a type II superconductor with a critical temperature of about $10\,\mathrm{K}$ [25]. The casing is a hollow cylinder with radius of about $35\,\mathrm{mm}$ and height $120\,\mathrm{mm}$. The resonator was then mounted on one end on a strip of copper, such that there is almost no copper close to the resonator anymore. The resonator itself is then aligned vertically, having the z-axis of the cylinder casing parallel to the resonators spiral plane. Two antenna made of semi-rigid copper coax cable were fed through the casing roof with two bore holes and then brought close to the pads of the resonator. At the end of the antennas roughly one centimeter of the copper shield was removed from the cable such that the signal can be transmitted and received. A picture of this setup can be seen in Figure 4.5a. Before the assembly could be put into the coldhead, the NbTi casing had to be wrapped into thick copper bands to ensure a good thermalization as shown in Figure 4.5b. Otherwise the casing might not get below its critical temperature or only after a

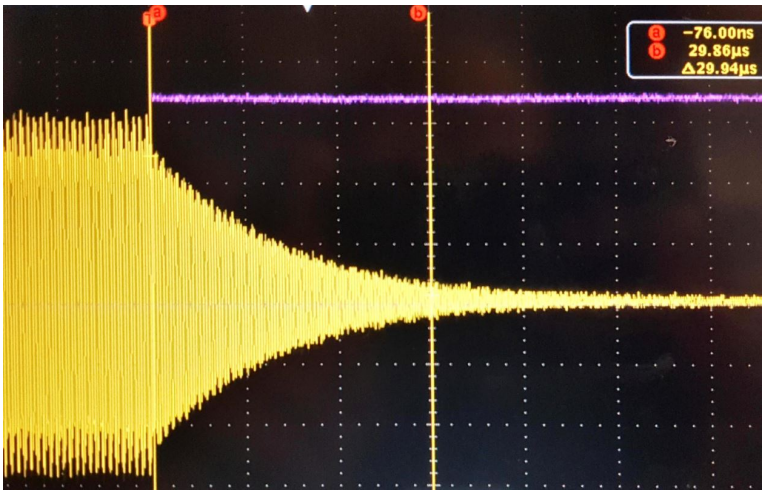

(a)

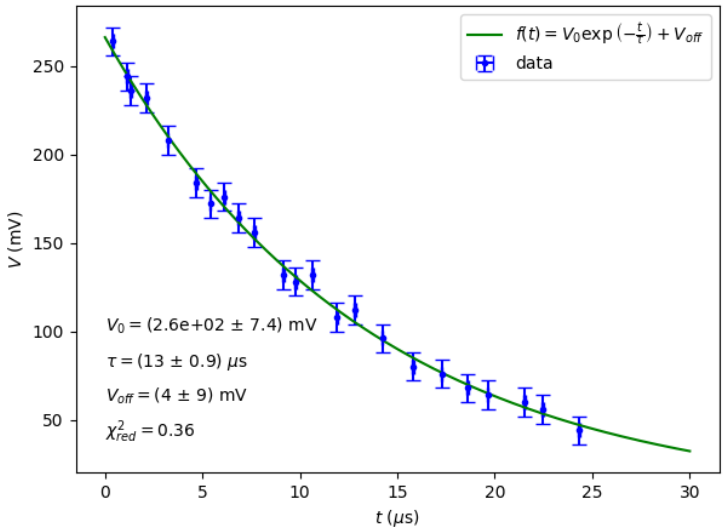

(b)

Figure 4.4: Ring down measurement of the second iteration. (a) Shows a picture of the oscilloscope triggered on the decay of the signal. The pink line representing the sync-signal starts at the position of the trigger-marker T. (b) Shows a fit to the datapoints recorded with the oscilloscope.

long time. Measurements similar as those described in the second interation were performed.

$$Q^{(3)} \approx 15800 \tag{4.1.13}$$

$$\nu_0^{(3)} \approx 82.152\,\mathrm{MHz} \tag{4.1.14}$$

$$Q_{\mathrm{rd}}^{(3)} = 16260 \pm 180 \tag{4.1.15}$$

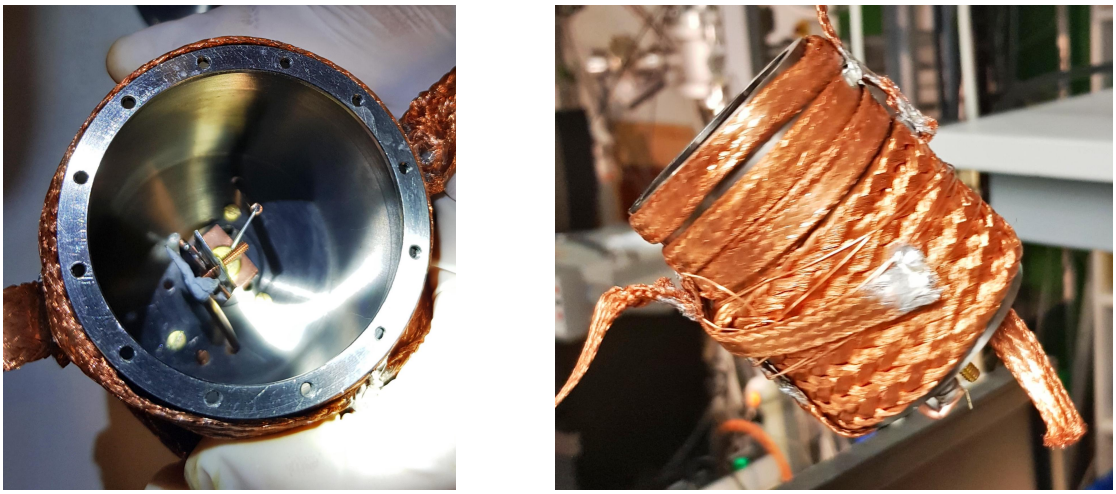

(a) (b)

Figure 4.5: (a) shows a picture of the inside of the setup in the NbTi casing. (b) shows the thick copper bands used to ensure a good thermal contact to the NbTi

The Q-value increased significantly, which most probably is due to the reduction of copper in the critical cylinder around the resonator, as has been estimated in chapter 3. During the warmup, a LabView-program was used to record data of the resonance curves and the temperature continuously. From these the change of the Q-value and the resonance frequency can be tracked. The plot for the change of the Q-value was combined with a plot of a later measurement and will be described then. The resonance frequency in Figure 4.6 can be observed to steeply decrease after the temperature surpassed the critical temperature of the YBCO.

Due to the increasing equivalent series resistance of the RLC-circuit and because of the transition of the YBCO from the superconducting to the normal conducting state, the damping constant γ increases, which then changes the resonance frequency according to

$$\omega_0^{\text{damped}} = \sqrt{\omega_0^2 - \gamma^2} \quad . \tag{4.1.16}$$

Additionally to this the inductance can also change after the YBCO becomes normal conducting, because the skin depth of the flowing current changes.

After this measurement was done and the setup was back to room temperature the external permanent magnet setup, made out of strong neodym magnets, was put around the NbTi casing to measure possible effects of the magnetic field on the Q-value. To mount the magnets on the coldhead the casing had to be detached first and then lowered into the magnet setup and attached there. Next to the addition of the magnets, this was the only change made to later be able to exclude other sources than the magnetic field as the cause for a change in the Q-value. At the position of the resonator in the middle of the magnet

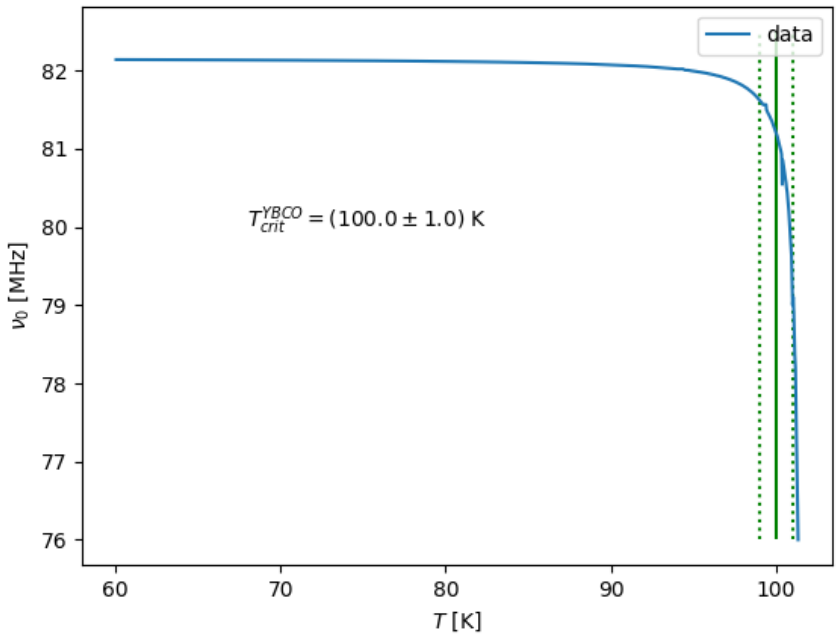

Figure 4.6: During the warmup of the third iteration the resonance frequency was plotted against the temperature. From this the transition temperature of YBCO can be estimated. The plot yields $T_{\text{crit}} = (100 \pm 1)$ K. Additionally to this an error of about 5 K can be estimated from uncertainties of the calibration and a temperature gradient from the sensor to the resonator. This shows a good agreement with the transition temperature of YBCO.

setup, the strength of the magnetic field is about $B = 280\,\text{mT}$ [22]. To identify a change of the Q-value more easily the data from the warmup with and without magnetic field are compared, which is done in Figure 4.7.

Here, one can see that the Q-value did not decrease significantly with the magnets installed. This seems to be reasonable because the magnetic field is aligned parallel to the resonators plane. In a normal conductor with the same dimensions this would mean that the material can not form large ring currents to compensate the magnetic field if turned on. Here the magnetic field is permanent and the material is superconducting, but in principle the parallel orientation offers less area to the exteriour magnetic field in which flux tubes can form oscillations, increasing the losses in the superconductor. A similar investigation has been conducted in Ref. [26] with the conclusion that the effect of the magnetic field is very weak for the parallel orientation, compared the the orthogonal orientation. The different behaviour of the Q-value can arise from the change of the setup. As explained before, the initial setup had to be detached for the measurement with the magnets. For high Q-values even small changes can have a severe impact on the measured result. Due to the massive magnetic setup the heat capacity of the setup is

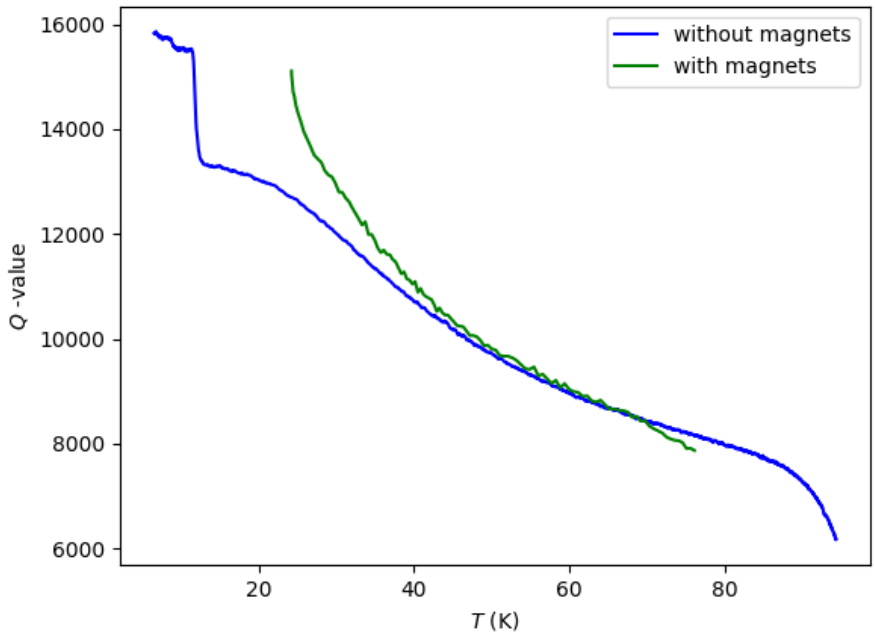

Figure 4.7: Measurement of the Q-value against temperature during the warmup process of the coldhead.

increased. Because of this the temperature measured by the sensor might not be exactly comparable to the setup measured without the magnetic setup. From the data without the magnets one can also notice the transition of the NbTi casing around $T = 10\,\mathrm{K}$. After this point the casing became non superconducting and the increased sheet resistance in this state caused an increase in the losses and therefore a lower Q-value. From the small height of the jump one can also see that the influences of the magnetic field are quite low at the position of the NbTi-casing, because the resistivity of the NbTi jumps by several orders of magnitude after the temperature increases to a higher value than the critical temperature [27].

4.2 Tests at the MPIK

In this subsection the setup and the measurement of one of the resonators designed in my "Projektpraktikum" is explained in detail. The chosen resonator is the one designed for the resonance frequency $\nu_0 = 27\,\mathrm{MHz}$. Because there are no holes in the sapphire substrate to fix the resonator with a screw like in Mainz, a dedicated clamping mechanism had to be manufactured, which clamps the resonator between two cut parts made out of FR4, as shown in Figure 4.8.

Directly above and below the resonator the FR4 material was cut out to reduce material in the cylinder of high influence estimated in chapter 3 and consequently decrease losses which would limit the Q-value.

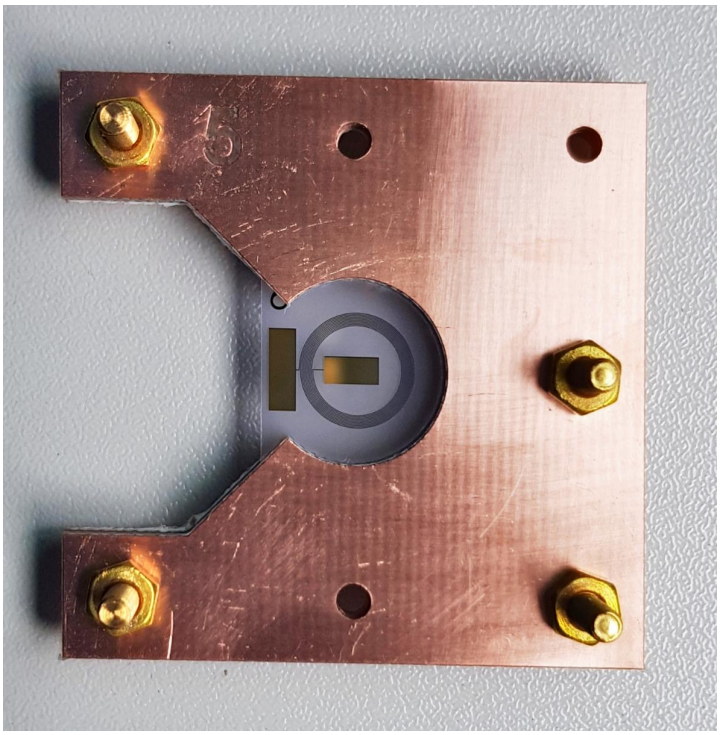

Figure 4.8: Resonator in a holder made out of FR4.

4.2.1 Tests in liquid nitrogen

Because the tests in Mainz were performed in a coldhead with each thermal cycle taking up one full day, the idea was first to test the resonator in liquid nitrogen which is at $T_{\mathrm{LN2}} = 77\,\mathrm{K}$, well below the critical temperature of YBCO. This should prevent the long waiting time, if the setup was directly immersed in liquid nitrogen. The main problem of such tests is the warmup phase. If the resonator is exposed to air while still below the dew point, water condensates on the surface of the resonator, increasing the risk that the YBCO degrades into a non-superconducting form [28]. To ensure that the superconductor does not come in contact with water, the test had to be performed in a pumped cavity. The basic measurement setup is the same as depicted in Figure 4.1a. The setup that was build can be seen in Figure 4.9.

In Figure 4.9a, one can see the copper casing, which has approximately the same dimensions as the NbTi casing used in Mainz and therefore should not limit the Q-value to low values. The two antennas, made of semi-rigid coax cable, sticking into the inside of the copper casing were fixed by soldering the copper shield of the coax cable onto the copper plate below the casing. The casing itself is fixed with a brass screw onto this copper plate and the plate is fixed onto the outer flange. Above and below the copper plate some thick copper mesh was squeezed into the available space to ensure a good thermal connection between the outside and the casing. Additionally to this, a PT1000 temperature sensor was installed.

(a) (b) (c)

Figure 4.9: (a,b) Shows pictures of the copper housing inside of the nitrogen setup. (c) Shows the total setup that will be almost totally submerged in liquid nitrogen.

The sensor was put into the copper mesh between the copper plate and the copper casing. The two signal wires of the antenna and the wire from the PT1000 were fed through individual electrical feed-through ports which can be seen in Figure 4.9c. It was ensured that the shield of the coax cable is well connected to the outside made out of steel to reduce unintentional cross-talk from the cables. The antenna inside of the casing were then positioned to be close to the resonator, which was mounted on the lid of the copper casing. The resonators plane was then oriented vertical, like in the setup in Mainz. Before the setup was closed (see Figure 4.9c) the lid with the resonator was put on top of the open copper casing (depicted in Figure 4.9b). The resonator was now inside of the closed casing and the antenna were close to the pads of the resonator. The setup was then closed and connected on one side to a scroll vacuum pump to evacuate the setup to $1 \times 10^{-2}\,\mathrm{mbar}$. Now it was put into a dewar filled with liquid nitrogen, such that all parts below the electrical feed-throughs are submerged. Several test were performed with adjustments of the antenna, but no resonance curve was visible on the network analyzer. A reason for this could be misaligned antennas. If the antenna are too far away from the resonator or the resonator is turned, such that the holding additionally shields some part of the resonator from the antenna then the received signal could be completely dominated by the existing cross-talk of the wires. In principle this setup should work, because it does not differ from the setups made in the coldhead. It would be a lot faster than a coldhead and one does only need liquid nitrogen which is more easily accessible than a coldhead. It would also allow measurements in the $77\,\mathrm{K}$ environment, which would suffice for this resonator design. Because of this it could be useful to revisit this setup. To ensure the antenna are oriented correctly one would need to mount the resonator on the bottom of the casing.

4.2.2 Tests in the coldhead

Since the tests in liquid nitrogen did not yield data on the performance of my design, it was then tested in the coldhead like in Mainz. The only difference is that there was no NbTi-Casing available. The resonator was mounted on a copper stripe, such that it is hanging below the middle of the coldhead without anything else in close proximity than the two antenna. The antennas are again coax cables, with the shield and isolation removed at the end close to the resonator. These coax cables are not semi-rigid, so they can move between different setups. The first test of the resonator was already successful and yielded the following values for the resonance frequency and the Q-value:

$$\nu_0 \approx 141.79\,\mathrm{MHz} \tag{4.2.1}$$

$$Q \approx 15000 \tag{4.2.2}$$

The resonance frequency is about a factor of five higher than $27\,\mathrm{MHz}$, which is the frequency it was designed for. The reason for this is that one needs a parallel capacitance of $C_p = 20\,\mathrm{pF}$ to achieve the designed frequency. In this measurement, this capacity was not implemented and therefore only the self-capacitance accounts for the calculation. This capacitance is assumed to be at least one order of magnitude lower than the trap capacitance, which then results in a too large resonance frequency. From this test one can also see that the cylinder of low influence was a good estimation to achieve a high Q-value, because it seems as if there is a lot of copper very close to the resonator as depicted in Figure 4.8, but there the field is too weak to cause major losses and the Q-value stays high.

After the warmup the coldhead was opened too early because of a malfunctioning temperature sensor. Some water condensated on top of the resonator and it quickly had to be put into vacuum to dry. Because of this, a second test with this resonator was performed, to see whether it was severly damaged. For this test the resonance curve can be seen in Figure 4.10.

The resonance frequency did only change by about $10\,\mathrm{kHz}$, but the Q-value decreased by 3000, resulting in

$$\nu_0 \approx 141.80\,\mathrm{MHz} \tag{4.2.3}$$

$$Q \approx 12000 \quad . \tag{4.2.4}$$

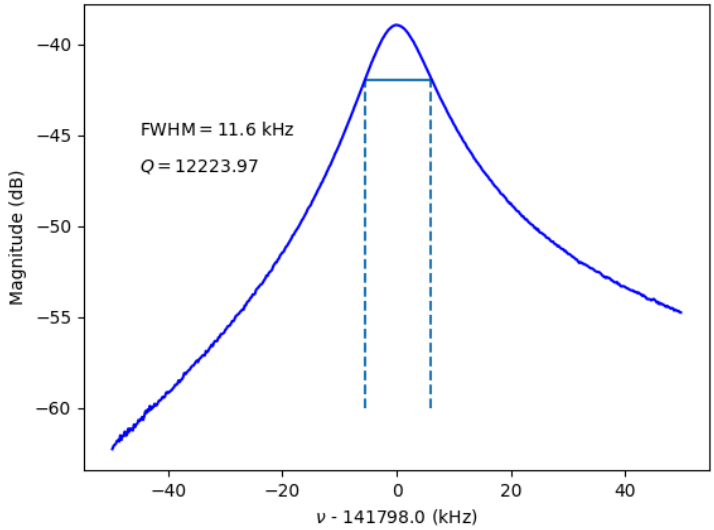

Figure 4.10: Resonance curve from the second measurement of the 27 MHz resonator

The decrease of the Q-value can be explained by two factors. On the one hand the properties of the YBCO could be worse than in the previous test, if the water did destroy some parts of the structure. On the other hand it was mentioned that the antenna are not semi-rigid and can change in position relatively to the resonator from test to test. This change can also worsen or improve the Q-value depending on how much of the shield is inside of the cylinder of high influence. It is assumed that the second case is more plausable from the appearance of the resonance curve and the still high Q-value.

5 The cryogenic amplifier

In this chapter, the requirements for an amplifier in the detection system are described shortly and the results at room temperature are presented.

5.1 Principle and requirements

The main purpose of the amplifier is to make the signal coming from the induced ion current of a few fA measureable. A high amplification as well as low noise is desired. This can be achieved by a cascade of amplifiers. Here, the amplification given in dB adds up and the noise of the previous stage(s) gets amplified stage and added to the noise of the current stage [29]. Because of this, a low noise is needed for the first amplifier in this cascade, because this noise will be amplified by all amplifiers further down the line.

The amplifier was build in adaptation to Ref. [30] as depicted in Figure 5.1.

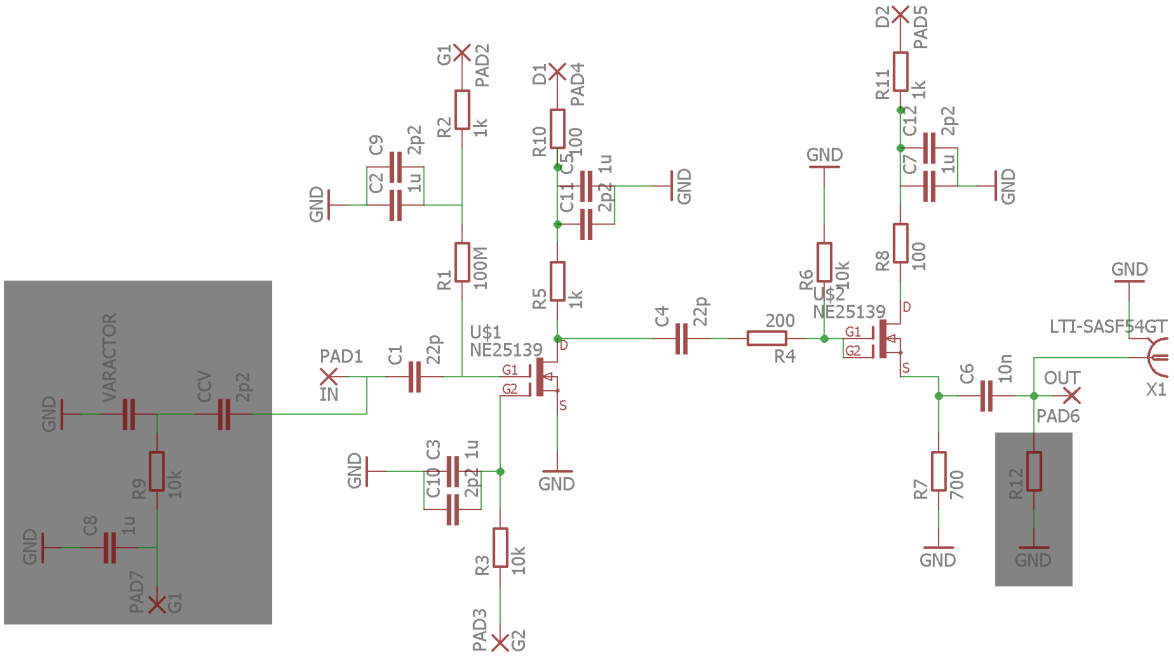

Figure 5.1: Scematic of the amplifier adapted from Ref. [30]. The gray areas are not populated yet.

For this design two field-effect-transistors (FET) were used. The first FET on the left is used to amplify the input signal. The second part with the other FET on the right is called a source follower and is used for impedance matching. This is useful to reduce reflections in the circuit, because most electronics have an input impedance of $50\,\Omega$.

5.2 Implementation and tests

The PCB designed according to the scematic depicted in Figure 5.1 was produced with a PCB milling machine. Lots of vias were implemented in the board design to ensure that the ground plane on the bottom of the board is well connected. The ground plane was then soldered onto a copper plate which then offers some room to be connected to the setup via some drill holes. During the assembly of the amplifier care was taken that all resistors and capacitors are suitable for cryogenic use. The final amplifier can be seen in Figure 5.2.

Figure 5.2: The assembled cryogenic amplifier. Starting from right side with the pink cable the cables are in clockwise order: Drain Stage1, Output, Drain Stage2, Gate2 Stage1, GND, Gate1 Stage1, Input

To test the amplifier Gate 1 (PAD2) of the first stage was connected to a voltage of about $V_{\mathrm{G1}} \approx -0.7\,\mathrm{V}$. Gate 2 (PAD3) was connected to GND or $V_{\mathrm{G2}} = 0\,\mathrm{V}$. Both drains (PAD4 + PAD5) are connected to the voltage $V_{\mathrm{D}} \approx 7.4\,\mathrm{V}$. Port 1 of the network analyzer, from which the signal is sent to the amplifier, is connected to PAD1 and the output of the amplifier (PAD6) is connected to port 2 of the network analyzer. To avoid saturating the amplifier, a $40\,\mathrm{dB}$ attenuation was put between port 1 and the input of the amplifier. From this setup Figure 5.3 was taken, which is already corrected for the $40\,\mathrm{dB}$ attenuation.

One can see that this cryogenic amplifier yields an amplification at room temperature of about

$$A = (14 \pm 0.5)\,\mathrm{dB}\ @\ 30\,\mathrm{MHz} \quad . \tag{5.2.1}$$

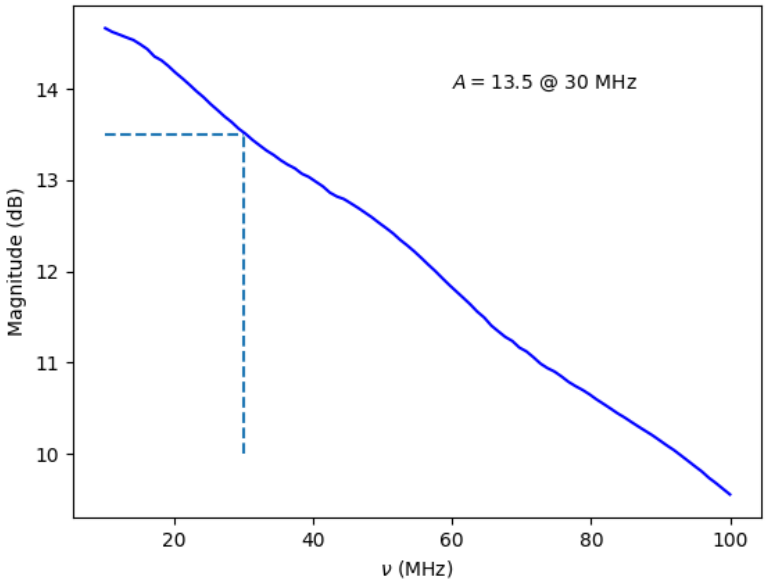

Figure 5.3: Frequency response of the amplifier at room temperature

The error was estimated by changing the voltages applied at the gates and drains and observing the change of the amplification. The data was taken from the setting which seemed to give the highest amplification. Before the amplifier can be used the amplification first has to be tested at $4\,\mathrm{K}$. Additionally to this, the voltage noise level should also be tested in this environment. Ideally this noise level should be low.

6 Results and outlook

In this work a new design for cyclotron resonators was presented and characterized. The new design is based on the lithographic production of a planar YBCO spiral placed on top of a sapphire substrate, which has a total area of only 1 to $2\,\mathrm{cm}^2$. This is manufactured by an external company saving time and promising more reproduciblity. The Q-value of the resonator was measured with a network analyzer and then also confirmed with a ring-down measurement. These measurements yielded Q-values as high as $Q = 16260 \pm 180$, which still might be limited by lossy material close to the resonator. From different iterations of the measurement and a simulation in COMSOL it could be estimated that a cylindrical shaped volume of radius $r = d_{\text{out}}$ and height $h = 2d_{\text{out}}$ centered at the resonator should be kept free of any materials which otherwise would cause higher losses. Together with the small size of the resonator with outer diameters of order $d_{\text{out}} = 1\,\mathrm{cm}$ this would make the total design small, fitting in a cylindrical volume of only $6\,\mathrm{cm}^3$. Additionally, the Q-value during the warmup-phase of the coldhead was observed with and without an exterior magnetic field. From this measurement one could see the transitions of the YBCO spiral and the NbTi-casing from supercoducting to normal conducting and conclude that the magnetic field has no visible effect at the given strength of $B = 280\,\mathrm{mT}$ with a parallel orientation of the field lines to the resonators plane. These results are very promising, showing that cyclotron resonators can be improved in many aspects. Additionally to the cyclotron resonator a cryogenic amplifier was constructed and tested at room temperature. This test yielded an amplification of $A = (14 \pm 0.5)\,\mathrm{dB}$ at $30\,\mathrm{MHz}$. The amplification and noise level has to be tested in the $4\,\mathrm{K}$ environment, before it can be used together with the resonator in the experiment.

Within this work, the first tests on the new design were made, but there are still many left to follow. In the future, tests in higher magnetic fields of a few tesla will be conducted to assure that this design also works in magnetic field typical for Penning trap experiments. Revisiting the tests in liquid nitrogen will also yield high Q-values which can be seen in the warmup measurements. This will make cyclotron resonators available in environments that cannot be cooled down to $4\,\mathrm{K}$. It will be interesting to measure the self-capacitance and inductance of the different designs and compare the inductances to the expected ones. If it can further be shown that also the inductances of designs with different resonance frequencies are more predictable than the helical resonators, cyclotron resonators can be pushed from hardly obtainable to more easily replaceable measurement components, boosting flexibility and bringing new ideas which need high Q-values nearer.

A Appendix

A.1 Further information on the designing process

Given the targeted inductances calculated from the resonance frequency and the trap capacitance as shown in Table 1, parameters were searched to fit closely to these values. These parameters are the number of turns N, the outer diameter d_{out}, the width of the wire w and the spacing between two turns s. For this two additional boundary conditions were set. The outer diameter should be $d_{\text{out}} \leq 2\,\text{cm}$ to be small enough to fit into the experimental setup of ALPHATRAP. Additionally the inner area should be large enough to be able to fit the soldering pad inside. This yielded the following configurations of parameters:

ν_0^{solder} [MHz]	N	d_{out} [μm]	w [μm]	s [μm]	Design-Nr.
6.8	40	16000	50	50	1
17.9	24	11100	50	50	4
18.4	25	13000	100	50	5
20.4	15	10700	100	50	8
27	10	9000	50	50	2
28	10	8500	50	50	6

Table 3: Final parameters of the resonator spirals for the soldering design.

The final configuration is not unique and can change for a fixed target inductance, if other boundary conditions are set. For the calculation of the inductance L via the modified Wheeler formula for the octogonal spiral with the coefficients $K_1 = 2.25$, $K_2 = 3.55$ [19] and the vacuum permeability μ_0

$$L = K_1 \mu_0 \frac{N^2 d_{\text{avg}}}{1 + K_2 \rho} \quad . \tag{A.1.1}$$

The fill ratio $\rho = \frac{d_{\text{out}} - d_{\text{in}}}{d_{\text{out}} + d_{\text{in}}}$ and the average diameter $d_{\text{avg}} = 0.5(d_{\text{out}} + d_{\text{in}})$ can be calculated from the inner diameter given by

$$d_{\text{in}} = d_{\text{out}} - 2N(w + s) \quad . \tag{A.1.2}$$

In this case the octogonal shape was chosen, because it is closest to the circular shape, which was realized.

A.2 Capacitive coupling

Soldering directly onto the pads of the resonator has some risks. If one solders with temperatures higher than 160°C the oxygen in the YBCO starts to diffuse out of the material, causing the supraconductor to degrade into a state in which it loses its superconducting properties. Additionally due to the thin gold and

YBCO layers, one has to be cautious to not put any major force on the soldered cables, because otherwise these layers could easily break off. For this reason a design with capacitive coupling was made. Here an outer ring area and the inner circle of diameter d_{in} can be used for building capacitors with C_r and C_a as shown in Figure 2.2. The capacity should be large compared to the trap capacitance, to not influence the circuit too much, because the two capacitors are in series to the trap capacitance as shown in Figure A.1.

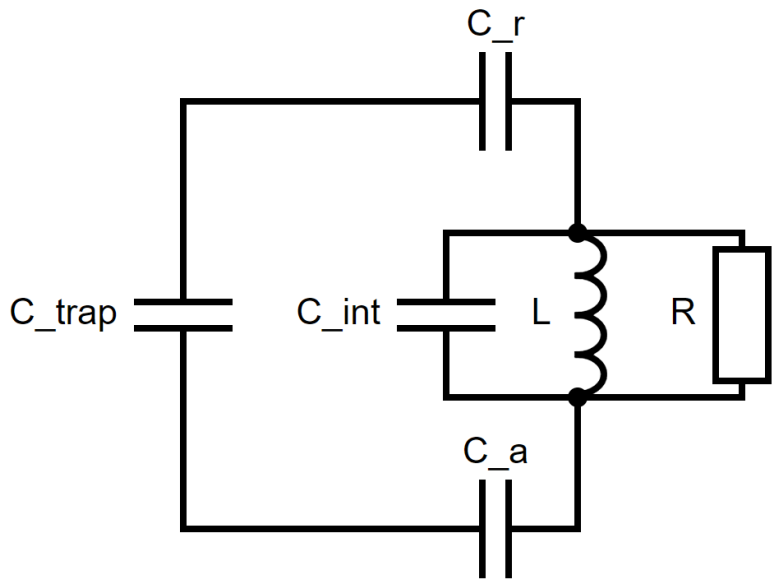

Figure A.1: Circuit for the capacitive coupling.

From this circuit one can calculate the total parallel capacitance C_{par} of the RLC-circuit with the additional condition $C_r \approx C_a$ to get

$$C_{\text{par}} = \frac{C_{\text{trap}}}{1 + 2\frac{C_{\text{trap}}}{C_{\text{r}}}} \quad . \tag{A.2.1}$$

With an assumed coupling capacitance of $C_r = 250\,\text{pF}$ the total parallel capacitance is changed and therefore the target inductance also has to change to yield the same resonance frequency. This coupling capacitance can be achieved with areas of size $A = 1\,\text{cm}^2$ and an isolating Kapton foil of thickness $d = 10\,\mu\text{m}$ and relative permittivity $\varepsilon_r = 3.4$ This was done for three designs shown in Table 4.

ν_0 [MHz]	C_r [pF]	L_target [nH]
17.9	9.26	7684
20.4	17.24	3177
27	17.24	1814

Table 4: Calculated target inductances for the design with capacitive coupling.

Together with the additional condition new parameters were found for this design, which are listed in Table 5.

ν_0 [MHz]	N	d_out [μm]	w [μm]	s [μm]	A [cm^2]	Design-Nr.
17.9	15	17500	50	50	1.65	3
20.4	10	17000	100	50	1.65	7
27	7	15900	50	50	1.54	9

Table 5: Final parameters of the resonator spirals for the design with capacitive coupling.

References

[1] S. Sturm, I. Arapoglou, A. Egl, M. Höcker, S. Kraemer, T. Sailer, B. Tu, A. Weigel, R. Wolf, J. C. López-Urrutia, and K. Blaum, "The ALPHATRAP experiment," *European Physical Journal: Special Topics*, vol. 227, pp. 1425–1491, 2 2019.

[2] C. Roux, C. Böhm, A. Dörr, S. Eliseev, S. George, M. Goncharov, Y. N. Novikov, J. Repp, S. Sturm, S. Ulmer, and K. Blaum, "The trap design of Pentatrap," *Applied Physics B: Lasers and Optics*, vol. 107, pp. 997–1005, 6 2012.

[3] E. G. Myers, "The most precise atomic mass measurements in penning traps," *International Journal of Mass Spectrometry*, vol. 349-350, pp. 107–122, 9 2013.

[4] C. Roques-Carmes, N. Rivera, J. D. Joannopoulos, M. Soljačić, and I. Kaminer, "Nonperturbative Quantum Electrodynamics in the Cherenkov Effect," *Physical Review X*, vol. 8, p. 041013, 10 2018.

[5] L. S. Brown and G. Gabrielse, "Geonium theory: Physics of a single electron or ion in a Penning trap," *Rev. Mod. Phys.*, vol. 58, pp. 233–311, Jan 1986.

[6] S. W. Kreim, "Direct Observation of a Single Proton in a Penning Trap," *Dissertation Universität Mainz*, 2009.

[7] M. Vogel, "Particle Confinement in Penning Traps," *Springer Series on Atomic, Optical, and Plasma Physics*, vol. 100.

[8] P. Micke, S. Kühn, L. Buchauer, J. R. Harries, T. M. Bücking, K. Blaum, A. Cieluch, A. Egl, D. Hollain, S. Kraemer, T. Pfeifer, P. O. Schmidt, R. X. Schüssler, C. Schweiger, T. Stöhlker, S. Sturm, R. N. Wolf, S. Bernitt, and J. R. C. López-Urrutia, "The Heidelberg compact electron beam ion traps," *Review of Scientific Instruments*, vol. 89, 6 2018.

[9] J. R. C. L. pez Urrutia, J. Braun, G. Brenner, H. Bruhns, C. Dimopoulou, I. N. Dragani, D. Fischer, A. J. G. lez Mart nez, A. Lapierre, V. Mironov, R. Moshammer, R. S. Orts, H. Tawara, M. Trinczek, and J. Ullrich, "Progress at the Heidelberg EBIT," *Journal of Physics: Conference Series*, vol. 2, pp. 42–51, 1 2004.

[10] S. Sturm, F. Köhler, J. Zatorski, A. Wagner, Z. Harman, G. Werth, W. Quint, C. H. Keitel, and K. Blaum, "High-precision measurement of the atomic mass of the electron," *Nature*, vol. 506, pp. 467–470, 2014.

[11] T. Kaltenbacher, F. Caspers, M. Doser, A. Kellerbauer, and W. Pribyl, "Resistive cooling circuits for charged particle traps using crystal resonators," *Review of Scientific Instruments*, vol. 82, 11 2011.

[12] Private communication with Sven Sturm.

[13] E. Gao, S. Sahba, H. Xu, and Q. Y. Ma, "A superconducting RF resonator in HF range and its multi-pole filter applications," *IEEE Transactions on Applied Superconductivity*, vol. 9, pp. 3066–3069, 1999.

[14] T. Frello, "Structural and Superconducting Properties of High-T c Superconductors," tech. rep., 1999.

[15] "Data Sheet Properties of Sapphire." `https://rayotek.com/PDF/Sapphire-Properties-Data-Sheet.pdf`. Accessed on 2022-07-22.

[16] "Data Sheet Properties of different metals." `https://www.engineeringtoolbox.com/thermal-conductivity-metals-d_858.html`. Accessed on 2022-07-22.

[17] "Low Temperature Properties of Materials." `https://uspas.fnal.gov/materials/10MIT/Lecture_1.2.pdf`. Accessed on 2022-08-07.

[18] J. Krupka, K. Derzakowski, M. Tobar, J. Hartnett, and R. G. Geyer, "Complex permittivity of some ultralow loss dielectric crystals at cryogenic temperatures," *Meas. Sci. Technol*, vol. 10, pp. 387–392, 1999.

[19] S. S. Mohan, M. D. M. Hershenson, S. P. Boyd, and T. H. Lee, "Simple Accurate Expressions for Planar Spiral Inductances," *IEEE JOURNAL OF SOLID-STATE CIRCUITS*, vol. 34, p. 1419, 1999.

[20] "Ceraco ceramic coating GmbH." `https://www.ceraco.de/`. Accessed on 2022-06-08.

[21] "AG Smorra / STEP." `https://antimatter.physik.uni-mainz.de/`. Accessed on 2022-08-07.

[22] D. Popper *PhD Universität Mainz*, proposed for 2024.

[23] C. Vijayakumar, M. Brightson, S. Rayar, and P. Selvarajan, "Development of $YBa_2Cu_3O_{7-\delta}$ superconducting thick film on Ba_2SmSbO_6 substrate material synthesised by combustion technique," *Journal of Experimental Nanoscience*, vol. 9, pp. 525–532, 5 2014.

[24] S. Hunklinger, *Moderne Thermodynamik Band 1 Physikalische Systeme und ihre Beschreibung*. 2018.

[25] D. Patel, S.-H. Kim, W. Qiu, M. Maeda, A. Matsumoto, G. Nishijima, H. Kumakura, S. Choi, and J. H. Kim, "Niobium-titanium (Nb-Ti) superconducting joints for persistent-mode operation," *Scientific Reports*, vol. 9, p. 14287, 12 2019.

[26] S. Ohshima, K. Kitamura, Y. Noguchi, N. Sekiya, A. Saito, S. Hirano, and D. Okai, "Surface resistance of YBCO thin films under high DC magnetic fields," *Journal of Physics: Conference Series*, vol. 43, pp. 551–555, 6 2006.

[27] A. Kushino, S. Kasai, S. Kohjiro, S. Shiki, and M. Ohkubo, "Development of Superconducting Coaxial Cables for Cryogenic Detectors," *Journal of Low Temperature Physics*, vol. 151, pp. 650–654, 5 2008.

[28] K. Yokota, T. Kura, M. Ochi, and S. Katayama, "Degradation of High-Temperature Superconductor $YBa_2Cu_3O_{7-x}$ in Water," *Japanese Journal of Applied Physics*, vol. 29, pp. L1425–L1427, 8 1990.

[29] J. J. Carr, *Radio Receiver Basics*. Elsevier, 2000.

[30] S. Ulmer, K. Blaum, H. Kracke, A. Mooser, W. Quint, C. C. Rodegheri, and J. Walz, "A cryogenic detection system at 28.9 MHZ for the non-destructive observation of a single proton at low particle energy," *Nuclear Instruments and Methods in Physics Research, Section A: Accelerators, Spectrometers, Detectors and Associated Equipment*, vol. 705, pp. 55–60, 3 2013.

Acknowledgements

I would like to thank Sven Sturm for the time he took to help me with questions and problems that I had and for giving me the opportunity to work at such an interesting topic. I learned very much during our discussions.

Further I also would like to thank the members of ALPHATRAP and PENTATRAP, especially Tim Sailer and Jost Herkenhoff for giving me lots of support during all phases of the thesis.

I also greatly enjoyed the time in Mainz working together with Fatma Abbass under the supervision of Christian Smorra.

Lastly I want to thank my parent for the support the gave to me.

Erklärung

Ich versichere, dass ich diese Bachelor-Arbeit selbstständig verfasst und nur die angegebenen Quellen und Hilfsmittel verwendet habe.

Heidelberg, den 08.08.2022,